Research Article | Vol. 29, No. 6 / 15 March 2021 / Optics Express 8160
Optics EXPRESS

Ultrabroadband, compact, polarization independent and efficient metasurface-based power splitter on lithium niobate waveguides

AMGED ALQULIAH,[1,2] MOHAMED ELKABBASH,[3,4,6] JIHUA ZHANG,[3,5] JINLUO CHENG,[1,2,7] AND CHUNLEI GUO[3,*]

[1]GPL, Changchun Institute of Optics, Fine Mechanics and Physics, Chinese Academy of Sciences, Changchun 130033, China
[2]University of Chinese Academy of Sciences, Beijing 100039, China
[3]The Institute of Optics, University of Rochester, Rochester, New York 14627, USA
[4]Present address: The Research Laboratory of Electronics, Massachusetts Institute of Technology, Cambridge, MA 02139, USA
[5]Present address: Nonlinear Physics Centre, Research School of Physics, The Australian National University, Canberra, ACT 2601, Australia
[6]melkabba@ur.rochester.edu
[7]jlcheng@ciomp.ac.cn
[*]guo@optics.rochester.edu

Abstract: We propose a metasurface-based Lithium Niobate waveguide power splitter with an ultrabroadband and polarization independent performance. The design consists of an array of amorphous silicon nanoantennas that partially converts the input mode to multiple output modes creating multimode interference such that the input power is equally split and directed to two branching waveguides. FDTD simulation results show that the power splitter operates with low insertion loss (< 1dB) over a bandwidth of approximately 800 nm in the near-infrared range, far exceeding the O, E, S, C, L and U optical communication bands. The metasurface is ultracompact with a total length of 2.7 μm. The power splitter demonstrates a power imbalance of less than 0.16 dB for both fundamental TE and TM modes. Our simulations show that the device efficiency exhibits high tolerance to possible fabrication imperfections.

1. Introduction

Research efforts towards miniaturization of optical elements are motivated by the drive to produce on-chip photonic devices that attain the advantages of electronics, e.g., nanoscale dimensions, and retain the advantages of photonics, e.g., low power consumption and broad bandwidth. However, a common trade-off is sacrificing the efficiency of a given device for the sake of miniaturization which, from a practical standpoint, is usually unacceptable [1]. Fragmented demonstration of a standalone device, not integrated with a complex system, can curtail the effect of efficiency drop. Practically, however, a small increase in the losses of a given device can render it dysfunctional. In the past few years, a new paradigm emerged in nanophotonics that promises to overcome this trade-off, namely, metasurfaces. Metasurfaces provide near complete control over the propagation of light through abrupt phase changes at an interface which is induced by deeply subwavelength antennas [1–5]. These metasurfaces offer the possibility to create ultrathin and efficient optical devices [6–12].

In the context of integrated photonic circuits (IPCs), minimizing the footprint of the main elements of such circuits, e.g., power splitters, polarizers, directional couplers, etc., is important to increase the cost-effectiveness and packing density of IPCs. Recently, chip-integrated metasurfaces platform translated the concept of a metasurface into IPCs, serving as a paradigm for versatile, compact, and complete control over waveguide optical signals. Several chip-scale

#415676 https://doi.org/10.1364/OE.415676
Journal © 2021 Received 25 Nov 2020; revised 6 Jan 2021; accepted 14 Jan 2021; published 2 Mar 2021

Optics EXPRESS

metasurface-based applications were recently demonstrated such as mode converters [1,4,13–16], mode-pass polarizers [17,18], polarization rotator [1], wavelength/polarization (de)multiplexers [19–21], asymmetric power transmitter [1], optical routers [22,23], and guided waves-to free space wave-couplers [24–26]. These metasurface designs have the potential to obtain high efficiency and miniaturized optical elements for future IPCs.

In this work, we demonstrate an ultracompact, ultrahigh efficiency, polarization independent and ultrabroadband power splitter using an array of amorphous-Si metasurface nanorods superimposed on a Lithium Niobate (LN) waveguide. Our device has an unprecedented ultra-broadband operation of 800 nm far exceeding the O, E, S, C, L, and U optical communication bands, and a total length of 2.7 μm. The device has excellent efficiency with low insertion loss of < 1 dB and a power imbalance of less than 0.16 dB for both fundamental TE and TM modes. The design is easy to fabricate and highly tolerant to fabrication deviations which makes it a reliable component in the chip-integrated photonic systems. We note that our concept can be realized in other dielectric material systems that support optical resonances.

2. Materials and methods

The device design is schematically illustrated in Fig. 1(a). The device consists of a LN waveguide with a thickness of 400 nm on top of a 2-μm buried SiO_2 layer, further supported on a single-crystal LN substrate [27]. The ridge LN waveguide has a trapezoidal cross-section with a width $d = 2600$ nm on the top, a sidewall tilting angle $\theta = 40$ degrees (considering the experimental implications of the LN waveguides [1,4]), a ridge height $h = 300$ nm and an under-etched slab thickness $s = 100$ nm (Fig. 1(b)) [1,4]. A metasurface consisting of an array of amorphous silicon (a-Si) nanorods (black rods) is superimposed on the waveguide (Fig. 1(a), inset). The Si-metasurface consists of 12 nanorods of a rectangular cross-section, patterned along the center top surface of the LN ridge waveguide and oriented along the y axis, with width w=75 nm, thickness $T = 130$ nm, center-to-center distance between the adjacent nanorods $\Lambda = 250$ nm, and a range of lengths (1.4, 1.4, 1.3, 1.1, 0.8, 2, 2, 0.8, 1, 1.4, 0.6, 0.3) μm. The nanorods length is varied to optimize for the power splitting figures of merit (FOMs), e.g., insertion loss, power imbalance between two output waveguides, and operation bandwidth. Following the seminal works on metasurface-based integrated photonic devices [1,4], in our work, we used the direct design approach to create the metasurface structure [28]. The dimensions of nanoantennas were parametrically swept to realize the desired optical response and to achieve the obtained device FOMs. The metasurface is ultracompact with a total length of L_x=2.7 μm. The designed waveguide and a-Si nanoantennas are coated with a 3-μm SiO_2 layer to ensure a polarization independent power splitting (see Supplement 1, Section 1 for more details). The suggested fabrication method is provided in Supplement 1, Section 2.

Figure 1(b) schematically illustrates the operation principle of the metasurface-based power splitter. As light propagates in the waveguide, its evanescent field interacts with the nanoantennas resulting in a spatially dependent abrupt phase change in addition to the propagation phase. An intuitive understanding of the device mechanism is as follows: the wave-antenna interaction partially converts the input fundamental mode to higher order modes which interferes with the input mode creating an effective multimode interferometer. Through multimode interference, images of the input mode are formed along the propagation direction of the waveguide. We note that in the near-infrared wavelengths range, a-Si has a refractive index ($n_{a-Si} \sim 3.45$) significantly higher than LN ($n_{LN} \sim 2.2$) (see Supplementary Figs. S3a, b) which strengthens the interaction between waveguide modes and Mie resonance modes in the a-Si nanoantennas. Moreover, we note that the anisotropic nature of LN waveguides has been taken into account in all of our simulations (see Supplement 1, Section 3). The use of dielectric antennas instead of plasmonic antennas minimizes the absorption losses.

Optics EXPRESS

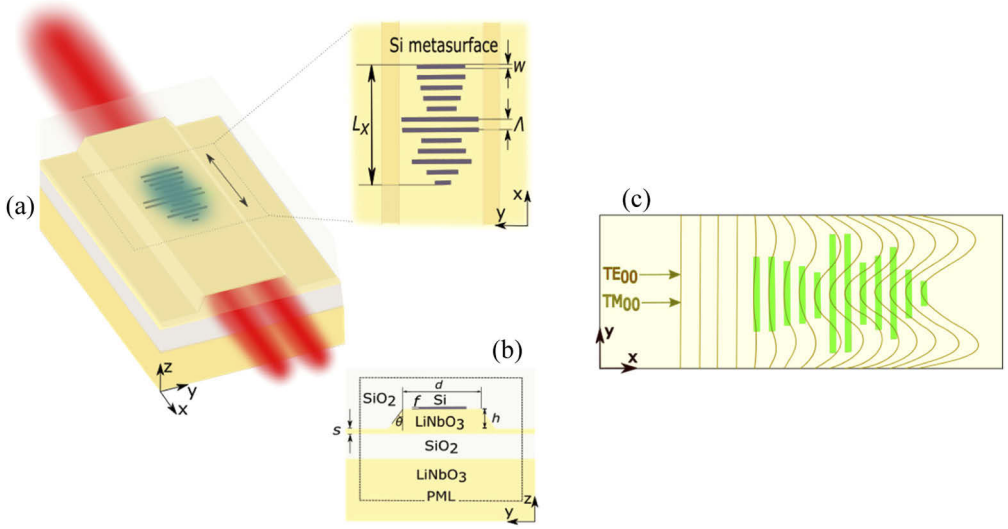

Fig. 1. Concept and schematic of the metasurface-based $LiNbO_3$ power splitter. (a). A 3D rendering of the device operating in the near infrared region. Inset (top right) showing the top view and dimensions of the metasurface consisting of an array of amorphous silicon nanorods (black rods) patterned on LN waveguide. (b). Schematic showing the cross-section of the device. (c). Conceptual diagram of the device operation principle showing that the mode-antenna interaction leads to a constructive interference of the guided mode at the center of the waveguide.

3. Results and discussion

Figure 2(a) and Fig. 2(b) show the calculated electric field $|E|$ flow profiles along the propagation at a wavelength λ=1550 nm at the XZ, and XY planes when the TM_{00} mode is injected along the propagation direction (x-axis) from left to right. Note that we purposely show the electric field profile in the stem waveguide without considering the output branches in order to ensure that the beam splitting occurs because of the interaction between the input mode with the designed metasurface, as opposed to other mechanisms, e.g., branching waveguide and Y-junction [29–31], where the splitting happens due to the sharp electric field discontinuity at the branches intersection thus causing relatively high mode mismatch loss and excess power leakage (see Supplement 1, Section 4) [32,33]. Figure 2(c) shows the $|E|$ for the fundamental TM_{00} mode in the power splitting device at λ=1550 nm when the LN waveguide is connected to two branches having width d_{out} = 1.2 μm. The output power takes relatively confined path along the output branches with a uniform splitting ratio and high transmittance.

In order to characterize the device performance, we studied the following figures of merit (FOM): insertion loss described as IL = -10log($|s_{21}|^2$ +$|s_{31}|^2$), where s_{21} and s_{31} are the complex parameters of transmission extracted from the fundamental mode of the input (port1) to the fundamental modes of the output ports (2 and 3); imbalance (IB), defined as the power variation between the two output ports relative to the input power IB = 10 log($|s_{21}|^2/|s_{31}|^2$); reflectance (R) and scattering (S) [34,35]. These FOM were calculated using 3D EMEsimulation (Lumerical Inc.) as a function of the wavelength. Figure 2(D) shows calculated transmittance (T) at the two output waveguides, the reflectance (R) and the scattering (S) for the TM_{00} mode over the simulated wavelength range. The calculated insertion loss for TM_{00} polarized light is less than 1 dB over the simulated wavelength range from 1.2 μm to 2 μm. Our simulations indicate for λ>2 μm, the corresponding intrinsic losses of the waveguide, as well as the calculated dispersion

Optics EXPRESS

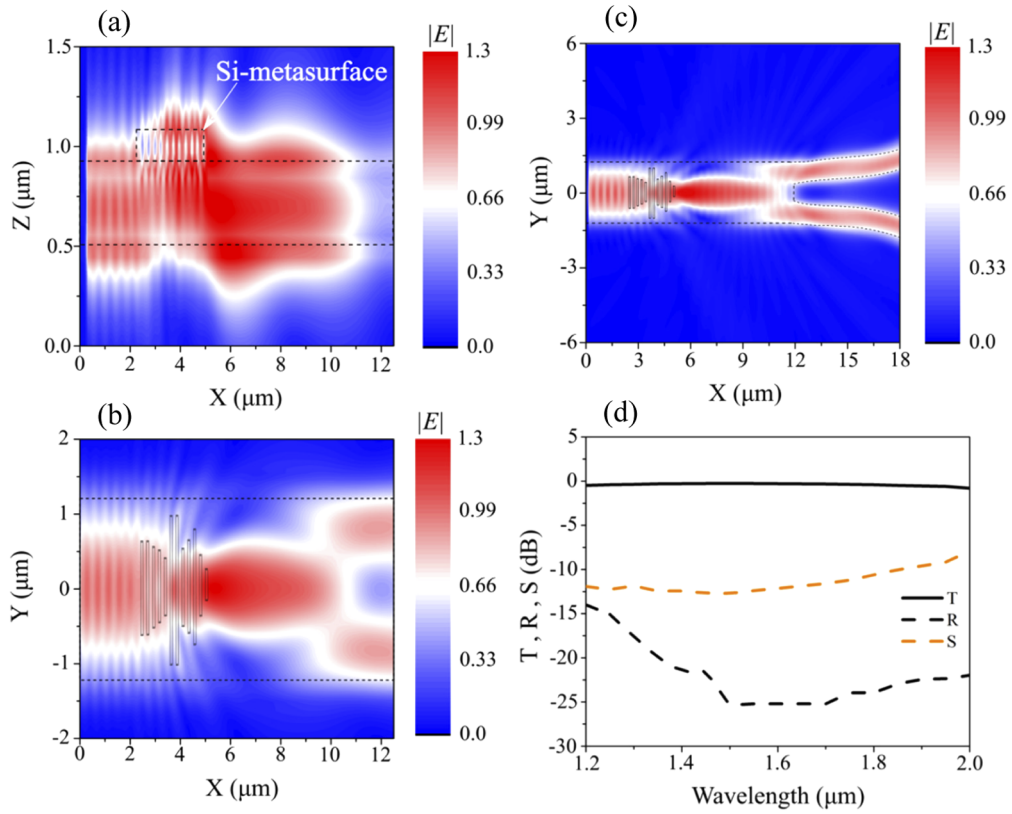

Fig. 2. Simulated device performance for TM_{00} mode. (a), and (b), Simulated field flow profiles $|E|$ (arbitrary units) along the propagation for the fundamental TM mode at λ=1550 nm at the center of LN waveguide at the (a) XZ, and (b) XY planes. (c). Full-wave simulation showing $|E|$ for the fundamental TM mode in the power splitting device at λ=1550 nm. The boundaries of LN waveguide and Si metasurface are indicated by dashed lines and rectangles, respectively, in the figures. Note that in (a) and (b) there are no output waveguides. (d), Calculated transmittance (T) at the two output waveguides (solid lines), reflectance (dashed black lines) and scattering (dashed orange lines) for the TM_{00} mode over the simulated wavelength range.

Optics EXPRESS

in the near-infrared region, rise appreciably. Moreover, it is expected that the propagation losses also increase for increasing wavelength. Hence, the total losses of the waveguide will eventually become too large (>1 dB) to allow for efficient guiding of the optical signal. This limits the performance of the splitter towards longer wavelengths. For λ<1.2 μm the reflected optical power rises gradually as a result of increasing the impedance mismatch by the Si metasurface (Fig. 2(d)). The device also shows an imbalance IB < 0.16 in the simulated wavelength range. The simultaneous excitation of higher order modes following the interaction between the input fundamental mode and the metasurface breaks the adiabatic condition and cause slight deviation in the splitting ratio. These results highlight the significant technological relevance of our proposed metasurface based power splitter.

Figure 3(a) and Fig. 3(b) show the calculated electric field $|E|$ flow profiles along the propagation at a wavelength λ=1550 nm at the XZ, and XY planes when the TE_{00} mode is injected along the propagation direction (x-axis) from left to right. Figure 3(c) shows the $|E|$ for the fundamental TE in the power splitting device at λ=1550 nm. Figure 3(d) shows the calculated transmittance (T) at the two output waveguides, the reflectance, and the scattering for the TE_{00} mode over the simulated wavelength range. We note that the results in Fig. 3(a)–(d) are nearly identical to the results obtained for the TM_{00} mode. Our design shows a polarization insensitive, record high power splitting bandwidth of 800 nm (~100 THz), a remarkably low insertion loss and imbalance, and a small footprint. A comparison with existing power splitters regarding all FOMs is shown in Table 1.

Table 1. Comparison with state-of-the-art power splitters

Design principles	Bandwidth (nm)	Insertion loss (dB)	Power Imbalance (dB)	Footprint (μm)	Polarization independent
Inverse design [36]	100	0.5	<10.0	3	
Adiabatic splitter [37]	100	0.31	0.2	300	
Particle swarm optimization [38]	100	0.28	0.02	2	
Photonic crystal [39]	30	0.25	0.58	20	No
Star coupler [40]	90	<1	<1	0.75	
SWG MMI [34]	500	<1	<1	25.4	
SWG adiabatic coupler [41]	185	0.11	0.7	35	
Si Modal slotted waveguide [42]	390	<1	<1	200	
SIN modal slotted waveguide [43]	420	<1	<1	320	
Adiabatic tapers based variational Y-junction [33]	70	0.19	0.47	20	Yes
Si-bent directional couplers [44]	80	<1	<0.9	50	
Our work	**800**	**<1**	**0.16**	**2.7**	

Figure 4(a) shows the normalized amplitude of the output modes for input fundamental TE and TM modes at 1.55 μm. Following the interaction with the metasurface, part of the input fundamental TE and TM mode is converted, mainly, to an output TE_{20} mode and TM_{20} mode, respectively. The interference between these modes with the remainder of the fundamental mode is responsible for the observed power splitting. In other words, the designed metasurface is functionally similar to a multimode interferoemeter. Figure 4(b) shows the normalized amplitude of the output modes for an input TE_{00} mode over a wide wavelength range. The mode conversion from a TE_{00} mode to a TE_{20} mode through the metasurface is obtained over the entire wavelength range which highlights the origin of the broadband operation of our power splitter. Section 5 in Supplement 1 includes simulation structure and further details on the mode analysis.

Optics EXPRESS

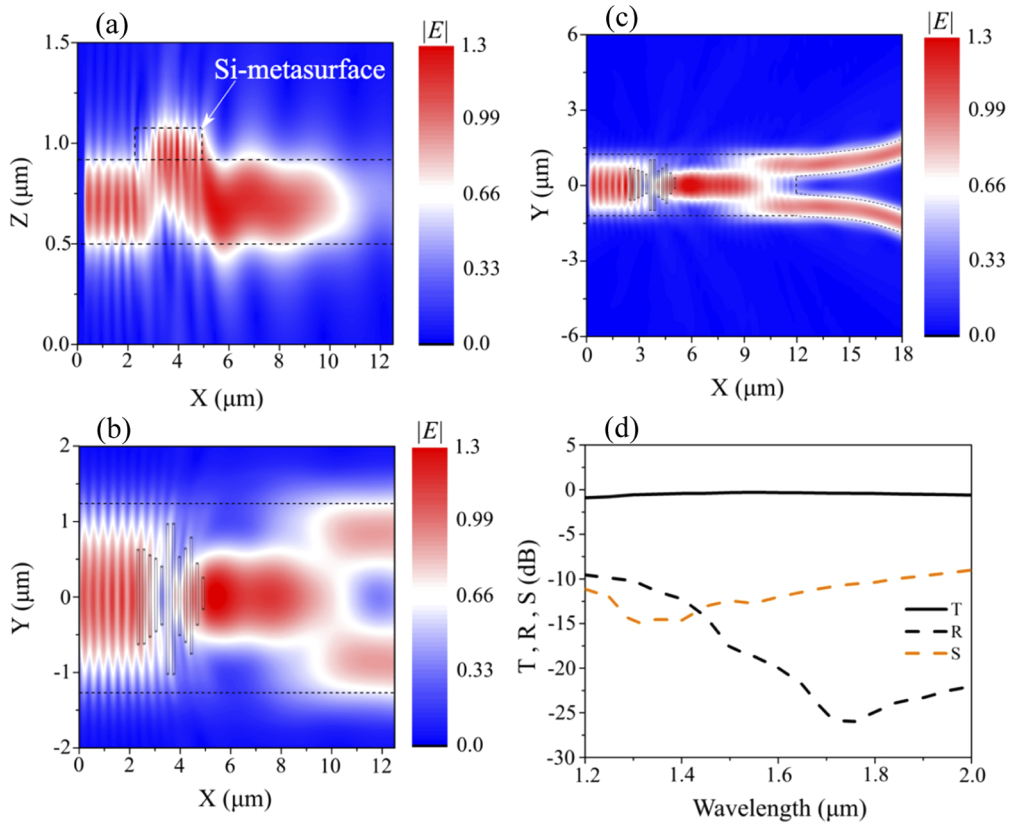

Fig. 3. Simulated device performance for TE_{00} mode. (a), and (b), Simulated field $|E|$ flow profiles along the propagation (arbitrary units) for the fundamental TE mode at λ=1550 nm at the center of LN waveguide at the (a) XZ, and (b) XY planes. (c). Full-wave simulation showing $|E|$ for the fundamental TE mode in the power splitting device at λ=1550 nm. The boundaries of LN waveguide and Si metasurface are indicated by dashed lines and rectangles, respectively, in the figures. Note that in (a) and (b) there are no output waveguides. (d) Calculated transmittance (T) at the two output waveguides (solid lines), reflectance (dashed black lines) and scattering (dashed orange lines) for the TE_{00} mode over the simulated wavelength range.

Optics EXPRESS

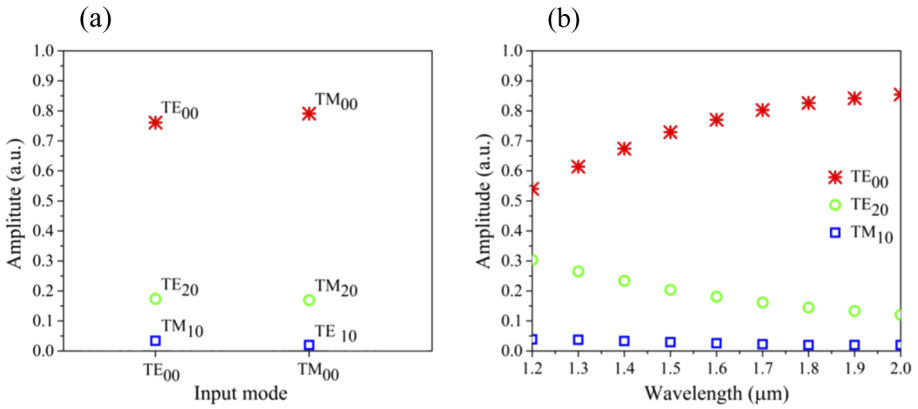

Fig. 4. Mode analysis at the end of stem waveguide. (a), Simulated amplitude of the output modes (forward propagation modes) at the end of the stem LN waveguide at λ=1550 nm. Note that the amplitudes of output modes resulted from both polarized input TE_{00} and TM_{00} light are nearly identical. (b) Amplitudes of the output modes as a function of wavelength when the TE_{00} is injected in the device. The broadband TE_{00}-to-TE_{20} and TM_{00}-to-TM_{20} mode conversion through the metasurface highlights the origin of the broadband operation of our power splitter

To ensure that our power splitter maintains the input fundamental TE_{00}/TM_{00} modes without exciting high-order modes at the output end, we analyzed the mode composition at the output end of the power splitter as shown in Fig. 5. Note that the results from analyzing the mode composition in both outputs of the device are nearly identical. Hence, for brevity, we show the results in one output port.

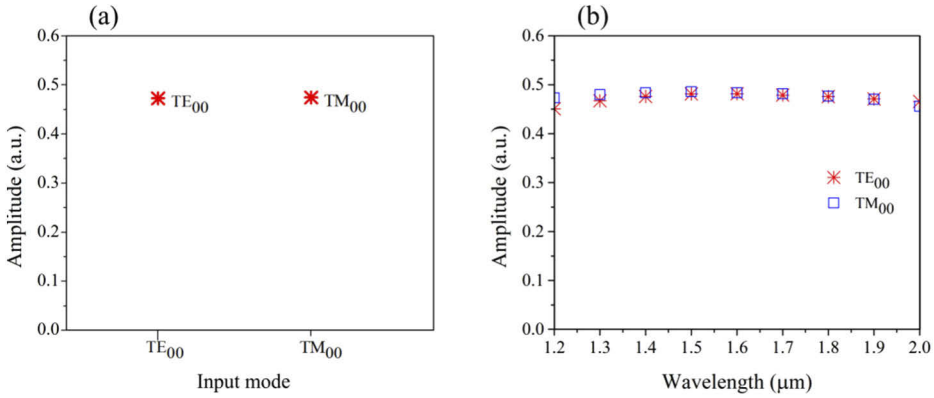

Fig. 5. Mode analysis at an output branch of the power splitter. (a) Simulated amplitude of the output modes (forward propagation modes) at the output branch of the device at λ=1550 nm. Note that the amplitudes of output modes resulted from both polarized input TE_{00} and TM_{00} light are nearly identical. (b) Amplitudes of the output modes as a function of wavelength when the TE_{00}\TM_{00} is injected in the device.

It is important to note that the output wave in both branches does not experience any polarization rotation. Figure 6(a) and Fig. 6(b) show the electric field component E_z for TM_{00} mode and electric field component E_y for TE_{00} mode. The corresponding vector diagrams of the electric fields of the modes at the input and output of stem waveguide are shown in arrows in Fig. 6(a) and

Optics EXPRESS

Fig. 6(b). After interacting with the metasurface, both the TM_{00} and TE_{00} modes are split while retaining the polarization of electric field of the input fundamental mode as shown in Fig. 6(c) and Fig. 6(d), These results are shown without introducing the Y branches, i.e., they are entirely due to the metasurface. Figure s10 shows the $|E_z|/\sqrt{(|E_x|^2 + |E_y|^2 + |E_z|^2)}$ for TM_{00} mode and $|E_y|/\sqrt{(|E_x|^2 + |E_y|^2 + |E_z|^2)}$ for TE_{00} mode.

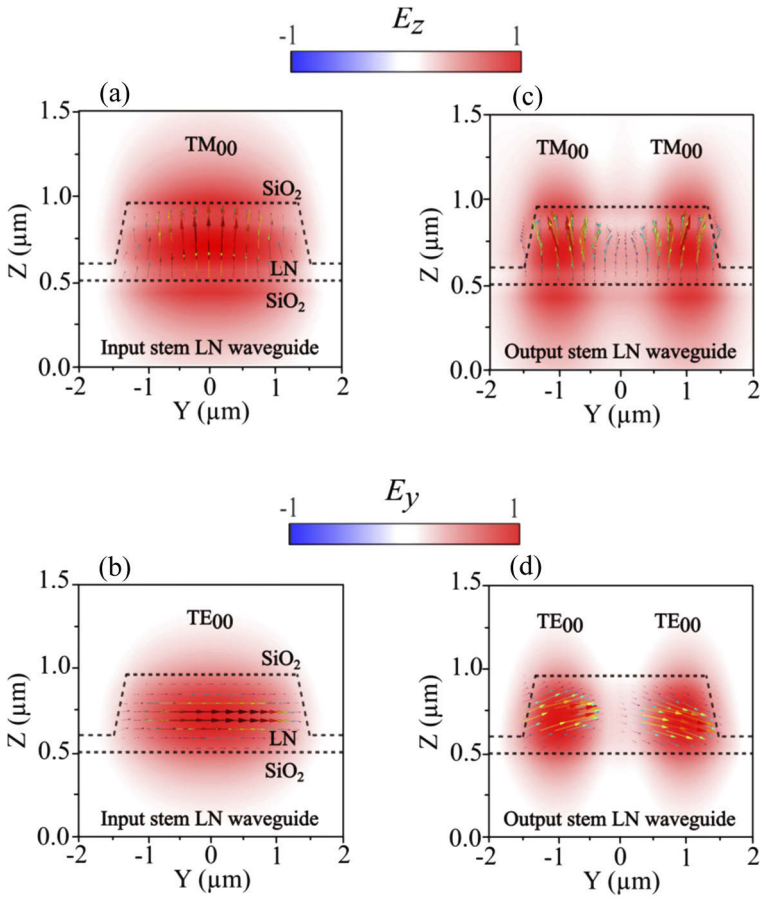

Fig. 6. Modes at the input and output ports of the stem LN waveguide at λ=1550 nm. (a), and (b), Plots of the E_z component for TM_{00} mode and E_y for TE_{00} mode of the input TM_{00} and TE_{00} modes. (c), and (d), Simulated output TM and TE modes after interacting with the metasurface. The arrows show the vector diagrams of the electric field component of the modes. The dashed lines indicate the boundaries of the LN waveguide.

We also would like to highlight the fabrication tolerance of our proposed metasurface waveguide power splitter. To illustrate that we calculate the IL considering variations in the waveguide thickness and width (Fig. 7(a)) and considering variations in the antenna thickness and width (Fig. 7(b)). Within the entire parameter space under consideration for both the waveguide and antenna dimensions, IL is lower than 1 dB. Regions of IL values lower than 0.28 dB correspond to design tolerance where the device efficiency is considerably high despite variations in the waveguide dimensions (Fig. 7(a)) or antenna dimensions (Fig. 7(b)).

Optics EXPRESS

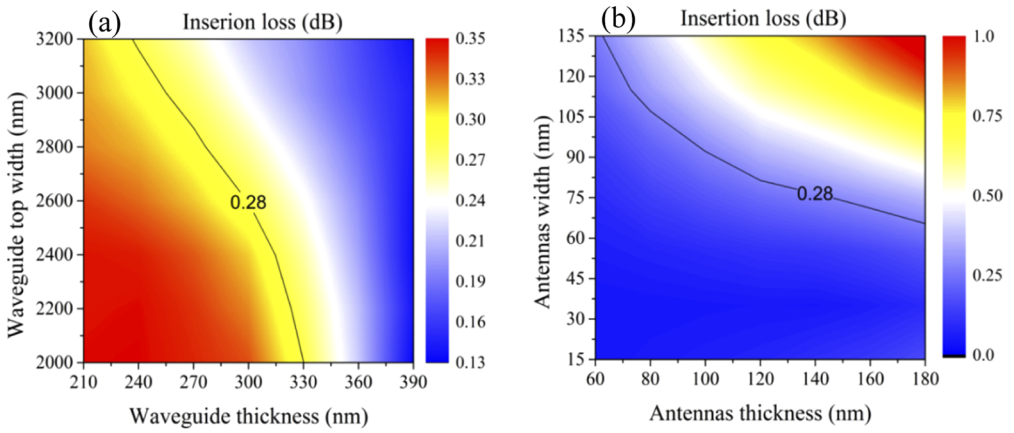

Fig. 7. Device fabrication tolerance. (a), and (b), Simulated device insertion loss for the TE_{00} mode at λ=1550 nm, considering the variation of the waveguide dimensions and antenna dimensions, respectively. The solid black lines in the contours denote the dimensions that do not alter the efficiency of the device.

4. Conclusion

In conclusion, we demonstrate a high efficiency LN waveguide power splitter using a-Si nanorod metasurface. The metasurface-based power splitter demonstrated a record bandwidth of 800 nm, while having a small footprint, low insertion loss and low imbalance. Our demonstration shows that metasurfaces interfaced with waveguides could provide simple and effective solution for miniaturized integrated photonic devices without sacrificing the device efficiency. The method utilized in our work can be used to realize other power divider designs, e.g., asymmetric y-splitters, symmetric 3-waysplitters, and 1×4 branching waveguides.

Funding. Scientific Research Project of the Chinese Academy of Sciences (QYZDB-SSW-SYS038); K. C. Wong Education Foundation (GJTD-2018-08); Bill and Melinda Gates Foundation (OPP1157723); CAS-TWAS president fellowship program.

Acknowledgments. We would like to acknowledge supports from Scientific Research Project of the Chinese Academy of Sciences (QYZDB-SSW-SYS038), K. C. Wong Education Foundation (GJTD-2018-08), and Bill & Melinda Gates Foundation (OPP1157723). A. A. acknowledges the CAS-TWAS presidents fellowship program.

M.E. initiated the project. C. G., M. E., and J. C. supervised the project. A. A. and M. E. designed the metasurface. A. A. performed simulations. A. A., M. E., J. Z. and, J. C. analyzed the data. A. A. and M. E. wrote the manuscript with inputs from all the authors. All authors discussed the research.

Disclosures. The authors declare no conflicts of interest.

Supplemental document. See Supplement 1 for supporting content.

References

1. Z. Li, M.-H. Kim, C. Wang, Z. Han, S. Shrestha, A. C. Overvig, M. Lu, A. Stein, A. M. Agarwal, M. Lončar, and N. Yu, "Controlling propagation and coupling of waveguide modes using phase-gradient metasurfaces," Nat. Nanotechnol. **12**(7), 675–683 (2017).
2. N. Yu, P. Genevet, M. A. Kats, F. Aieta, J.-P. Tetienne, F. Capasso, and Z. Gaburro, "Light Propagation with Phase Discontinuities: Generalized Laws of Reflection and Refraction," Science **334**(6054), 333–337 (2011).
3. D. Lin, P. Fan, E. Hasman, and M. L. Brongersma, "Dielectric gradient metasurface optical elements," Science **345**(6194), 298–302 (2014).
4. C. Wang, Z. Li, M.-H. Kim, X. Xiong, X.-F. Ren, G.-C. Guo, N. Yu, and M. Lončar, "Metasurface-assisted phase-matching-free second harmonic generation in lithium niobate waveguides," Nat. Commun. **8**(1), 2098 (2017).
5. Z. Wang, T. Li, A. Soman, D. Mao, T. Kananen, and T. Gu, "On-chip wavefront shaping with dielectric metasurface," Nat. Commun. **10**(1), 3547 (2019).
6. G. Zheng, H. Mühlenbernd, M. Kenney, G. Li, T. Zentgraf, and S. Zhang, "Metasurface holograms reaching 80% efficiency," Nat. Nanotechnol. **10**(4), 308–312 (2015).

Optics EXPRESS

7. T. Phan, D. Sell, E. W. Wang, S. Doshay, K. Edee, J. Yang, and J. A. Fan, "High-efficiency, large-area, topology-optimized metasurfaces," Light: Sci. Appl. **8**(1), 48 (2019).
8. J. Zhang, M. ElKabbash, R. Wei, S. C. Singh, B. Lam, and C. Guo, "Plasmonic metasurfaces with 42.3% transmission efficiency in the visible," Light: Sci. Appl. **8**(1), 53 (2019).
9. Z. Wei, X. Liu, and Y. Cao, "Switchable Metasurface With Broadband and Highly Efficient Electromagnetic Functionality.," Front. Phys. **8**, 90 (2020).
10. M. I. Shalaev, J. Sun, A. Tsukernik, A. Pandey, K. Nikolskiy, and N. M. Litchinitser, "High-Efficiency All-Dielectric Metasurfaces for Ultracompact Beam Manipulation in Transmission Mode," Nano Lett. **15**(9), 6261–6266 (2015).
11. J. Chunqi, Z. Jihua, and G. Chunlei, "Metasurface integrated with double-helix point spread function and metalens for three-dimensional imaging," Nanophotonics **8**(3), 451–458 (2019).
12. J. Joonkyo, P. Hyeonjin, P. Junhyung, C. Taeyong, and S. Jonghwa, "Broadband metamaterials and metasurfaces: a review from the perspectives of materials and devices," Nanophotonics **9**(10), 3165–3196 (2020).
13. H. Wang, Y. Zhang, Y. He, Q. Zhu, L. Sun, and Y. Su, "Compact Silicon Waveguide Mode Converter Employing Dielectric Metasurface Structure," Adv. Opt. Mater. **7**, 1801191 (2018).
14. D. Ohana and U. Levy, "Mode conversion based on dielectric metamaterial in silicon," Opt. Express **22**(22), 27617–27631 (2014).
15. S. Molesky, Z. Lin, A. Y. Piggott, W. Jin, J. Vucković, and A. W. Rodriguez, "Inverse design in nanophotonics," Nat. Photonics **12**(11), 659–670 (2018).
16. C. Yao, Y. Wang, J. Zhang, X. Zhang, C. Zhao, B. Wang, S. C. Singh, and C. Guo, "Dielectric Nanoaperture Metasurfaces in Silicon Waveguides for Efficient and Broadband Mode Conversion with an Ultrasmall Footprint," Adv. Opt. Mater. **8**(17), 2000529 (2020).
17. B. Wang, S. Blaize, and R. Salas-Montiel, "Nanoscale plasmonic TM-pass polarizer integrated on silicon photonics," Nanoscale **11**(43), 20685–20692 (2019).
18. Z. Xing, C. Li, Y. Han, H. Hu, Z. Cheng, and T. Liu, "Design of on-chip polarizers based on graphene-on-silicon nanowires," Appl. Phys. Express **12**(7), 072001 (2019).
19. A. Y. Piggott, J. Lu, K. G. Lagoudakis, J. Petykiewicz, T. M. Babinec, and J. Vučković, "Inverse design and demonstration of a compact and broadband on-chip wavelength demultiplexer," Nat. Photonics **9**(6), 374–377 (2015).
20. B. Shen, P. Wang, R. Polson, and R. Menon, "An integrated-nanophotonics polarization beamsplitter with 2.4×2.4 μm2 footprint," Nat. Photonics **9**(6), 378–382 (2015).
21. Y. Zhang, Z. Li, W. Liu, Z. Li, H. Cheng, S. Chen, and J. Tian, "Spin-Selective and Wavelength-Selective Demultiplexing Based on Waveguide-Integrated All-Dielectric Metasurfaces," Adv. Opt. Mater. **7**(6), 1801273 (2019).
22. C. Yao, S. C. Singh, M. ElKabbash, J. Zhang, H. Lu, and C. Guo, "Quasi-rhombus metasurfaces as multimode interference couplers for controlling the propagation of modes in dielectric-loaded waveguides," Opt. Lett. **44**(7), 1654–1657 (2019).
23. Y. Meng, F. Hu, Z. Liu, P. Xie, Y. Shen, Q. Xiao, X. Fu, S.-H. Bae, and M. Gong, "Chip-integrated metasurface for versatile and multi-wavelength control of light couplings with independent phase and arbitrary polarization," Opt. Express **27**(12), 16425–16439 (2019).
24. R. Guo, M. Decker, F. Setzpfandt, X. Gai, D.-Y. Choi, R. Kiselev, A. Chipouline, I. Staude, T. Pertsch, D. N. Neshev, and Y. S. Kivshar, "High–bit rate ultra-compact light routing with mode-selective on-chip nanoantennas," Sci. Adv. **3**(7), e1700007 (2017).
25. R. Guo, M. Decker, F. Setzpfandt, I. Staude, D. N. Neshev, and Y. S. Kivshar, "Plasmonic Fano Nanoantennas for On-Chip Separation of Wavelength-Encoded Optical Signals," Nano Lett. **15**(5), 3324–3328 (2015).
26. Y. Meng, F. Hu, Y. Shen, Y. Yang, Q. Xiao, X. Fu, and M. Gong, "Ultracompact Graphene-Assisted Tunable Waveguide Couplers with High Directivity and Mode Selectivity," Sci. Rep. **8**(1), 13362 (2018).
27. C. Wang, M. J. Burek, Z. Lin, H. A. Atikian, V. Venkataraman, I. C. Huang, P. Stark, and M. Lončar, "Integrated high quality factor lithium niobate microdisk resonators," Opt. Express **22**(25), 30924–30933 (2014).
28. M. M. Elsawy, S. Lanteri, R. Duvigneau, J. A. Fan, and P. Genevet, "Numerical Optimization Methods for Metasurfaces," Laser Photonics Rev. **14**(10), 1900445 (2020).
29. A. Sakai, T. Fukazawa, T. J. I. T. o, and E. Baba, "Low Loss Ultra-Small Branches in a Silicon Photonic Wire Waveguide," IEICE trans. electron. **85**, 1033–1038 (2002).
30. H. Yajima, "Dielectric thin-film optical branching waveguide," Appl. Phys. Lett. **22**(12), 647–649 (1973).
31. K. K. Chung, H. P. Chan, and P. L. Chu, "A 1×4 polarization and wavelength independent optical power splitter based on a novel wide-angle low-loss Y-junction," Opt. Commun. **267**(2), 367–372 (2006).
32. B. Desiatov, A. Shams-Ansari, M. Zhang, C. Wang, and M. Lončar, "Ultra-low-loss integrated visible photonics using thin-film lithium niobate," Optica **6**(3), 380–384 (2019).
33. Y. Wang, S. Gao, K. Wang, and E. Skafidas, "Ultra-broadband and low-loss 3 dB optical power splitter based on adiabatic tapered silicon waveguides," Opt. Lett. **41**(9), 2053–2056 (2016).
34. R. Halir, P. Cheben, J. M. Luque-González, J. D. Sarmiento-Merenguel, J. H. Schmid, G. Wangüemert-Pérez, D.-X. Xu, S. Wang, A. Ortega-Moñux, and Í Molina-Fernández, "Ultra-broadband nanophotonic beamsplitter using an anisotropic sub-wavelength metamaterial," Laser Photonics Rev. **10**(6), 1039–1046 (2016).
35. C.-C. Huang and T.-C. Sun, "Numerical simulations of tunable ultrashort power splitters based on slotted multimode interference couplers," Sci. Rep. **9**(1), 12756 (2019).

Optics EXPRESS

36. A. Y. Piggott, E. Y. Ma, L. Su, G. H. Ahn, N. V. Sapra, D. Vercruysse, A. M. Netherton, A. S. P. Khope, J. E. Bowers, and J. Vučković, "Inverse-Designed Photonics for Semiconductor Foundries," ACS Photonics **7**(3), 569–575 (2020).
37. J. Xing, K. Xiong, H. Xu, Z. Li, X. Xiao, J. Yu, and Y. Yu, "Silicon-on-insulator-based adiabatic splitter with simultaneous tapering of velocity and coupling," Opt. Lett. **38**(13), 2221–2223 (2013).
38. Y. Zhang, S. Yang, A. E.-J. Lim, G.-Q. Lo, C. Galland, T. Baehr-Jones, and M. Hochberg, "A compact and low loss Y-junction for submicron silicon waveguide," Opt. Express **21**(1), 1310–1316 (2013).
39. L. H. Frandsen, P. I. Borel, Y. X. Zhuang, A. Harpøth, M. Thorhauge, M. Kristensen, W. Bogaerts, P. Dumon, R. Baets, V. Wiaux, J. Wouters, and S. Beckx, "Ultralow-loss 3-dB photonic crystal waveguide splitter," Opt. Lett. **29**(14), 1623–1625 (2004).
40. G. Rasigade, X. Le Roux, D. Marris-Morini, E. Cassan, and L. Vivien, "Compact wavelength-insensitive fabrication-tolerant silicon-on-insulator beam splitter," Opt. Lett. **35**(21), 3700–3702 (2010).
41. H. Yun, L. Chrostowski, and N. A. F. Jaeger, "Ultra-broadband 2×2 adiabatic 3 dB coupler using subwavelength-grating-assisted silicon-on-insulator strip waveguides," Opt. Lett. **43**(8), 1935–1938 (2018).
42. D. González-Andrade, C. Lafforgue, E. Durán-Valdeiglesias, X. Le Roux, M. Berciano, E. Cassan, D. Marris-Morini, A. V. Velasco, P. Cheben, L. Vivien, and C. Alonso-Ramos, "Polarization- and wavelength-agnostic nanophotonic beam splitter," Sci. Rep. **9**(1), 3604 (2019).
43. D. González-Andrade, S. Guerber, E. Durán-Valdeiglesias, D. Pérez-Galacho, X. Le Roux, N. Vulliet, S. Cremer, S. Monfray, E. Cassan, D. Marris-Morini, F. Boeuf, P. Cheben, L. Vivien, A. V. Velasco, and C. Alonso-Ramos, "Ultra-wideband dual-polarization silicon nitride power splitter based on modal engineered slot waveguides," Opt. Lett. **45**(2), 527–530 (2020).
44. X. Chen, W. Liu, Y. Zhang, and Y. Shi, "Polarization-insensitive broadband 2×2 3 dB power splitter based on silicon-bent directional couplers," Opt. Lett. **42**(19), 3738–3740 (2017).